https://doi.org/10.5194/egusphere-2026-1772
Preprint. Discussion started: 29 April 2026

# Antagonism or synergy: Divergent surface water dynamics at the southern margin of the Eurasian permafrost

Bo Zhang[1], Tiantian Liao[1], Haitian Lu[2], Jianuo Li[1], Ziyan Huang[1], Jiuhui Li[1]*, Meng Guo[1]*

[1]Key Laboratory of Geographical Processes and Ecological Security of Changbai Mountains, Ministry of Education, School of Geographical Sciences, Northeast Normal University, Changchun, 130024, China
[2]School of Architecture and Urban Planning, Chongqing University, Chongqing, 400045, China

*Correspondence to*: Jiuhui Li (lijh801@nenu.edu.cn) and Meng Guo (guom521@nenu.edu.cn)

**Abstract.** Intensifying climate change and human activities are substantially altering frozen ground conditions, disrupting both surface water regimes and groundwater connectivity. The specific driving mechanisms behind these surface water shifts at the southern margin of the Eurasian permafrost, however, remain poorly quantified due to overlooked spatial heterogeneity. This study analyzed surface water dynamics in the Songhua River Zone (SHRZ) from 1988 to 2024 by integrating an improved water detection method with an interpretable geographical extreme gradient boosting framework coupled with shapley additive explanations. The results show a marked hydrological reversal from shrinkage to expansion around 2012. Expansion in the seasonal frozen ground region (24.77%) significantly outpaced that in the permafrost region (9.38%). Spatially explicit attribution identified a structural divergence in regulation mechanisms: the permafrost region is dominated by human activities (76.4%), forming an "antagonistic" pattern where reservoir-driven expansion is constrained by environmental barriers. In contrast, the seasonal frozen ground region is governed by natural factors (72.4%), exhibiting a "synergistic" pattern where climate and terrain jointly promote water expansion. Across distinct water types, natural factors control 93.6% of lake dynamics, whereas human activities dominate river systems (71.0%) and reservoirs (56.0%). Furthermore, this surface water expansion occurred alongside accelerated groundwater depletion, suggesting that the surface recovery was achieved at the expense of subsurface storage. These findings demonstrate that surface water expansion does not equate to water security, highlighting the need for targeted surface-groundwater management strategies and prospective research integrating dynamic permafrost degradation processes to further elucidate these ecohydrological trade-offs.

**Keywords:** Surface water dynamics; Geographical-XGBoost; SHapley Additive exPlanations (SHAP); Spatially explicit attribution; Permafrost margin

## 1 Introduction

Surface water plays an important role in maintaining biodiversity, supporting human well-being, and regulating local climate (Gardner et al., 2015; Zhou et al., 2025). However, intensifying climate change and human activities have disrupted hydrological cycles, thereby exacerbating the uncertainty of surface water distribution and persistence (Pekel et al., 2016; Samaniego, 2025). This uncertainty is particularly pronounced in frozen ground regions. Specifically, the permafrost layer functions as an impermeable barrier that hinders effective groundwater recharge, but its ongoing degradation is fundamentally altering soil permeability and hydrological flow paths (Frampton et al., 2013). The trade-off between this barrier effect and thaw intensity determines the hydraulic connectivity between surface water and deep groundwater. In contrast, seasonally frozen ground consistently maintains active vertical exchange during thaw periods (Woo and Winter, 1993). However, the spatially heterogeneous driving effects of climate, underlying surface characteristics, human activities, and other hydrological factors, as well as the consequent divergent surface water dynamics across different frozen ground regions, still lack systematic quantification (Wang et al., 2024). Therefore, unraveling the spatially explicit attribution of surface water dynamics provides a necessary scientific basis for adaptive water resource management along the southern permafrost margin.

Accurate hydrological monitoring is the prerequisite for understanding these complex dynamics. Although cloud computing platforms such as Google Earth Engine (GEE) have revolutionized large-scale monitoring (Tamiminia et al., 2020), existing global surface water products often exhibit considerable uncertainty in intensive agricultural regions like the Songhua River Zone (SHRZ) and frequently lack real-time monitoring capabilities (Wu et al., 2019). As a major national granary, this region features extensive croplands, which share high spectral similarity with natural water bodies during specific phenological stages. This spectral confusion frequently leads to the erroneous identification of farmland as surface water in conventional datasets, thereby significantly compromising the accuracy of long-term trend analysis. Mitigating this spectral confusion requires a multi-dimensional thresholding approach combined with rigorous environmental masking (Lu et al., 2024). Therefore, this study develops an improved open-surface water detection method with enhanced noise control (IOWDM-ENC). By synergizing strictly calibrated water and vegetation indices with dynamic topographic and impervious surface masks, this targeted scheme effectively isolates true water signals from agricultural and terrain-induced noise, providing a reliable observational foundation for subsequent analysis.

Situated at the southern margin of the Eurasian permafrost, the SHRZ is highly sensitive to climate change (Yang et al., 2025) and constitutes a strategic resource region for ecosystem and economic development in Northeast China (Lu et al., 2022). Although surface water area in the SHRZ has exhibited substantial shifts over recent decades (Liu et al., 2024), understanding the driving mechanisms remains challenging due to methodological limitations (Yu et al., 2021). Existing attribution analyses primarily rely on global statistical models or conventional machine learning (Liang et al., 2024; Song et al., 2025). However, these global-scale approaches often assume spatially stationary relationships, which inevitably average out local variations (Brunsdon et al., 1996). Crucially, a specific driver may exert a positive influence in one sub-region while acting as a constraint in another; aggregating these opposing effects neutralizes the signal and masks the true local mechanisms. Furthermore, while standard machine learning models effectively capture non-linear relationships, they suffer from a "black box" nature that restricts the understanding of why specific factors are dominant (Reichstein et al., 2019). To break through these limitations, spatially local machine learning algorithms have emerged as a promising solution. For instance, by embedding adaptive spatial kernels into gradient-boosting trees, the Geographical-XGBoost model can capture spatially varying relationships without sacrificing non-linear predictive power (Grekousis, 2025). Concurrently, incorporating game-theoretic approaches like SHapley Additive exPlanations (SHAP) can deconstruct the ML black box, explicitly quantifying whether a factor functions as a promoter or an inhibitor at any specific location (Lundberg and Lee, 2017).

Given the above background, this study attributes surface water dynamics in the SHRZ from 1988 to 2024 by constructing an interpretable Geographical Artificial Intelligence (GeoAI) framework that integrates the Geographical-XGBoost model with SHAP. This framework is applied to a high-precision dataset generated by IOWDM-ENC. The specific objectives are to: (1) quantify the spatially heterogeneous drivers of surface water change, overcoming the masking effects of global models; and (2) identify the distinct hydrological response patterns and regulation mechanisms in permafrost and seasonal frozen ground regions. This study aims to provide spatially explicit insights for adaptive water resource management at this climate-sensitive permafrost margin.

## 2 Materials and method

### 2.1 Study area

The SHRZ is situated in Northeast China and covers a total area of approximately $1.1 \times 10^6$ km² (Fig. 1). The region experiences a temperate monsoon climate with mean annual precipitation typically ranging from 500 to 800 mm, and mean annual temperature typically ranging from -4°C to 8°C (Li et al., 2014). In terms of geomorphology, the region exhibits a distinctive "horseshoe-shaped" structure, characterized by mountains on three sides encircling a central plain (Li et al., 2019). The mountainous regions are dominated by coniferous and broadleaf forests and wetlands that function as ecological barriers, whereas the central lowlands support extensive farmland, serving as a significant national production base for grain and economic crops (Wu and Zhang, 2018).

The SHRZ serves as a typical region along the southern margin of the Eurasian permafrost, where the distribution of frozen ground aligns closely with these topographic and vegetation gradients (Heginbottom et al., 2002). The permafrost region, primarily distributed in the northern Greater and Lesser Khingan Mountains, is characterized by high elevation, dense forest cover, and low permeability, with the frozen layer acting as an impermeable barrier (Jin et al., 2007). The seasonal frozen ground region, encompassing the southern plains and valleys, is instead defined by flat terrain and intensive agricultural activities. This geographical configuration lays the physical foundation for the divergent hydrological regulation mechanisms investigated in this study.

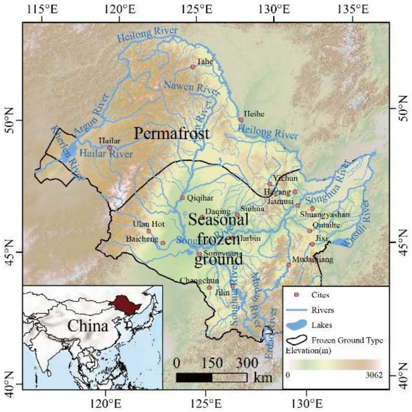

**Figure 1. Geographical location, elevation distribution and spatial division of frozen ground regions in the SHRZ. (Map source approval numbers: GS (2024) 0650 and GS (2021) 648).**

### 2.2 Data

#### 2.2.1 Landsat images

This study acquired all available Landsat 5/7/8/9 surface reflectance imagery on GEE covering the SHRZ from 1988 to 2024 (Fig. S1a-S1b). To minimize seasonal interference from ice and snow, images from the ice-free period (April to October) were selected annually. A strict quality control process was applied, masking clouds and shadows (cloud cover < 10%) (Foga et al., 2017). This filtering yielded 13,989 high-quality scenes, ensuring sufficient high-quality Landsat data were available for monitoring spatiotemporal surface water changes in the SHRZ (Fig. S1c-S1d).

#### 2.2.2 Climate, hydrological, and surface environmental factors

The selected natural factors were categorized into climate and environmental factors (CEF), as well as terrain and soil factors (TSF). The CEF represents a dynamic environmental state, integrating both meteorological forcings and hydrological processes. This category includes global water storage anomaly (GWSA), surface water availability (SWA), fractional vegetation cover (FVC), land surface temperature (LST), surface soil moisture (SSM), surface runoff (SR), sub-surface runoff (SSR), and snowmelt. In contrast, the TSF represents relatively static underlying surface conditions, including soil texture type (STT), elevation, and slope. Specifically, SR, SSR, and snowmelt were derived as annual cumulative values from the ERA5-Land Daily dataset, quantifying the depth water or water equivalent would have if spread evenly over the grid box. SWA was calculated by subtracting total terrestrial evapotranspiration from precipitation (Cui et al., 2022), and

STT was processed using One-hot encoding to handle categorical data (Zheng and Casari, 2018). Detailed data sources, resolutions, and references are provided in Table 1.

### 2.2.3 Human activity factors

Anthropogenic impacts were quantified using three human activity factors (HAF): new reservoirs (NR), human footprint (HF), and irrigated cropland area (ICA). The NR dataset specifically identifies reservoirs constructed since 2000. HF functions as a proxy for cumulative human pressure, integrating multi-source data including built environments, population density, nighttime lights, cultivated land, pastures, roads, railways, and navigable waterways. ICA represents the fractional coverage of cropland requiring irrigation within each grid cell. Detailed descriptions of these datasets are provided in Table 1.

**Table 1 Detailed description of driving factors used in this study.**

| Factors | Resolution | Time span | Dataset name | Reference |
|---|---|---|---|---|
| SWA | 1 km | 2000-2020 | 1- km monthly precipitation dataset for China<br>Penman-Monteith-Leuning Evapotranspiration V2 | (Peng et al., 2019; He et al., 2022) |
| GWSA | 0.05° | 2002-2022 | Global high-resolution water storage anomaly dataset | (Zhang et al., 2024) |
| FVC | 1 km | 2000-2020 | MOD13A2.061 Terra Vegetation Indices 16-Day Global 1km | (Huete et al., 1997; Didan, 2021) |
| LST | 1 km | 2000-2020 | MOD11A2.061 Terra Land Surface Temperature and Emissivity 8-Day Global 1km | (Wan et al., 2021) |
| SSM | 1 km | 2000-2020 | Global daily surface moisture dataset at 1-km resolution | (Zheng et al., 2023) |
| SR | 0.1° | 2000-2020 | ERA5-Land Daily Aggregated - ECMWF Climate Reanalysis | (Copernicus Climate Change Service, 2019) |
| SSR | 0.1° | 2000-2020 | ERA5-Land Daily Aggregated - ECMWF Climate Reanalysis | (Copernicus Climate Change Service, 2019) |
| Snowmelt | 0.1° | 2000-2020 | ERA5-Land Daily Aggregated - ECMWF Climate Reanalysis | (Copernicus Climate Change Service, 2019) |
| STT | 1 km | 2000-2018 | High resolution National Soil Information Grids of China | (Liu et al., 2022) |
| Elevation | 30 m | 2000 | NASA SRTM Digital Elevation 30m | (Farr et al., 2007) |
| Slope | 30 m | 2000 | NASA SRTM Digital Elevation 30m | (Farr et al., 2007) |
| HF | 30 m | 2000-2020 | Global Human Footprint dataset | (Mu et al., 2022) |
| NR | Vector | 2000-2020 | GREI-p2k | (Fan et al., 2024) |
| ICA | 250 m | 2000-2020 | CIrrMap250 | (Zhang et al., 2022; Zhang et al., 2024) |

## 2.3 Methods and data processes

### 2.3.1 Improved open-surface water detection method

Given the complex surface heterogeneity of the SHRZ, this study constructed a regionally tailored detection scheme known as the improved open-surface water detection method with enhanced noise control (IOWDM-ENC). The IOWDM-ENC advances the 'WI+VI' paradigm (Zou et al., 2018) through a dual-optimization strategy involving stricter spectral thresholds and comprehensive ancillary masking (Fig. 2). For the extraction index, this method introduces specific lower bounds for MNDWI and NDWI to suppress background noise effectively (Xu, 2006; Lu et al., 2023). Candidate water pixels are identified only when they satisfy the newly imposed constraints where $MNDWI > 0.1$, $NDWI > -0.1$, $EVI < 0.1$, and ($MNDWI > NDVI$ or $MNDWI > EVI$). The indexes are calculated as:

$$NDVI = \frac{\rho_{NIR} - \rho_{\mathrm{red}}}{\rho_{NIR} + \rho_{\mathrm{red}}} \tag{1}$$

$$EVI = 2.5 \times \frac{\rho_{NIR} - \rho_{\mathrm{red}}}{\rho_{NIR} + 6 \times \rho_{\mathrm{red}} - 7.5 \times \rho_{\mathrm{blue}} + 1} \tag{2}$$

$$NDWI = \frac{\rho_{\mathrm{green}} - \rho_{\mathrm{NIR}}}{\rho_{\mathrm{green}} + \rho_{\mathrm{NIR}}} \tag{3}$$

$$MNDWI = \frac{\rho_{\mathrm{green}} - \rho_{\mathrm{SWIR1}}}{\rho_{\mathrm{green}} + \rho_{\mathrm{SWIR1}}} \tag{4}$$

where $\rho_{red}$, $\rho_{green}$, $\rho_{blue}$, $\rho_{NIR}$, and $\rho_{SWIR1}$ represent the surface reflectance of the red light, green light, blue light, near-infrared, and short-wave infrared bands, respectively.

In addition to improving spectral extraction, the OWDM-ENC integrates a multi-source masking procedure to eliminate complex environmental noise (Tamiminia et al., 2020). This procedure includes the following: (1) a slope constraint (< 20°) derived from GMTED2010 (Danielson and Gesch, 2011), which physically precludes water accumulation in steep terrain; (2) an urban mask using GAIA data (Gong et al., 2020), which excludes impervious surfaces; and (3) a dynamic topographic shadow mask, which is calculated using solar azimuth and zenith angles to remove shaded areas caused by terrain relief (Lu et al., 2023).

### 2.3.2 Accuracy validation of surface water

This study evaluated the detection accuracy using high-resolution Sentinel-2 and Jilin-1 imagery as ground truth. A total of 15,000 validation points were established across the SHRZ based on a stratified random sampling design (Table S1, Fig. S2a). A confusion matrix was used as an evaluation tool for surface water detection accuracy (Olofsson et al., 2014), and the area estimation adjustment error method was applied to calculate the confidence interval of surface water area (Olofsson et al., 2013). In addition, this study compared the identification results of the original method, JRC global surface water (GSW) v1.4 data, and IOWDM-ENC for both 2016 and 2021 (Zou et al., 2018).

### 2.3.3 Classification of surface water components and types

Surface water components were delineated based on water frequency (WF), calculated as the ratio of water detections to total valid observations (excluding cloud, cloud shadow, and snow/ice) per year (Wu and Liu, 2015). Informed by the stability analysis of water pixel counts (Fig. S1d), pixels exhibiting 25% ≤ WF < 75% were categorized as seasonal surface water (SSW) (Rokni et al., 2015), whereas those with WF ≥ 75% were designated as permanent surface water (PSW) (Lu et al., 2024). These components were subsequently intersected with the 2020 CNLUCC dataset to distinguish three specific water types: river channel and floodplain (RCF), reservoir and pond (RP), and lake.

#### 2.3.4 Trend analysis methods

Temporal trends in surface water area (1988–2024) were quantified using linear regression models. To identify potential structural breakpoints in the time series, this study employed the cumulative sum (CUSUM) method. CUSUM detects abrupt changes by accumulating the deviations of observed values from the long-term mean; a significant excursion from zero indicates a shift in the mean level of the hydrological regime (Hawkins and Olwell, 1998). To investigate the temporal synchronization and potential response time scales between surface water dynamics and environmental drivers, cross-correlation analysis was performed with a maximum lag of 3 years (Box et al., 2016).

At the pixel scale, changes in water frequency (WF) were evaluated using the Theil-Sen slope estimator combined with the Mann-Kendall significance test (Sen, 1968), a non-parametric approach robust against data outliers. Based on the slope direction and statistical significance ($p < 0.05$), trends were categorized into five distinct classes: significant increase, insignificant increase, stable, insignificant decrease, and significant decrease. Finally, to normalize the disparity in water surface extent across different sub-regions, the magnitude of change was defined as the ratio of the area exhibiting significant WF shifts to the baseline surface water area in 1988.

#### 2.3.5 Geographical-XGBoost-SHAP attribution model

To quantify the long-term driving effects, significant trend slopes (2000–2020) for surface water and dynamic factors were calculated at the pixel level and aggregated into a 1 km grid to represent areal proportions. Multicollinearity was mitigated by excluding variables where Spearman correlation coefficients exceeded 0.7 (Dormann et al., 2013). Attribution analysis employed a dual-modeling strategy to distinguish between general dominance and local regulation mechanisms. First, a Global XGBoost model was trained to establish baseline feature importance. While robust for ranking drivers, this global approach assumes spatially stationary relationships, potentially masking localized feedback mechanisms where driver effects might invert across regions. Consequently, the Geographical-XGBoost model was implemented to resolve this limitation. By integrating adaptive spatial kernels into the gradient boosting framework, Geographical-XGBoost constructs localized sub-models that effectively capture the spatial non-stationarity of hydrological drivers (Grekousis, 2025). Model performance was evaluated using $R^2$, RMSE, and MAE.

To deconstruct the driving mechanisms, both models were coupled with SHapley Additive exPlanations (SHAP)

(Lundberg and Lee, 2017). Global importance was derived from the mean absolute SHAP values of the global model, ensuring an accurate ranking of driver magnitude. Spatial heterogeneity was examined using the spatially explicit SHAP values generated by Geographical-XGBoost. Unlike global metrics, this local approach retains the sign (positive or negative) of the contribution, thereby identifying distinct regulation patterns.

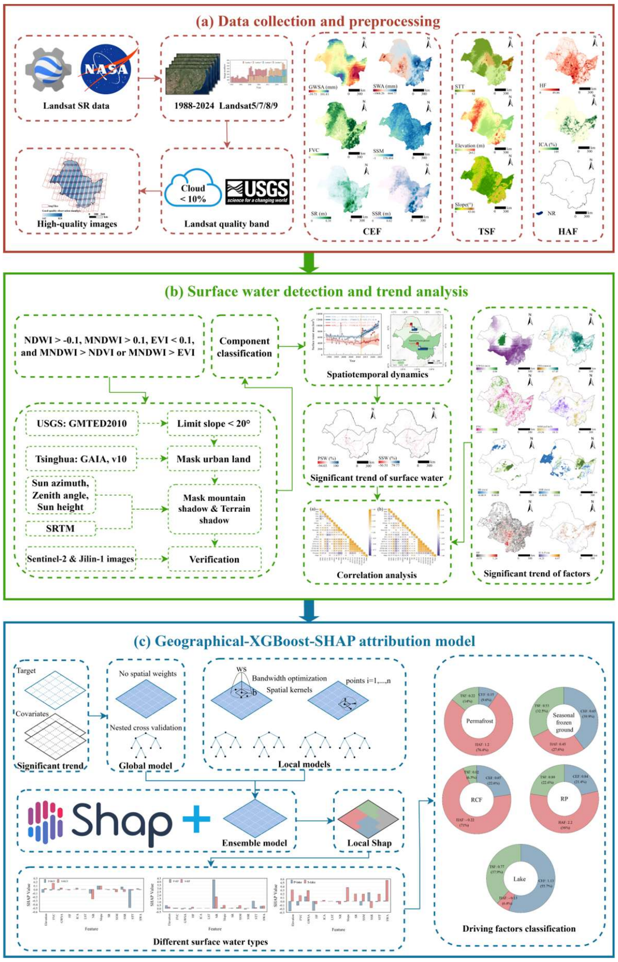

**Figure 2. Methodological framework. (a) Data collection and preprocessing; (b) Surface water detection and trend analysis; (c) Geographical-XGBoost-SHAP attribution model.**

## 3 Results

### 3.1 Accuracy verification of IOWDM-ENC

The IOWDM-ENC achieving an overall accuracy (OA) of 99.03%, with detailed confidence intervals provided in Fig. S2b. This performance marks a substantial improvement over the original method (94.66%), validating the necessity of the optimized thresholds and masking strategies. Compared to the JRC-GSW dataset (98.22%), the user's accuracy for surface water increased by 10.57% and the producer's accuracy by 12.6%. These results indicate IOWDM-ENC is more effective at suppressing agricultural noise and capturing smaller surface water in the SHRZ (Tables S2–S4).

While the overall Accuracy remains comparable to the JRC-GSW dataset, IOWDM-ENC offers a distinct advantage in temporal continuity. Unlike the JRC-GSW dataset, which is currently limited to historical records ending in 2021, the IOWDM-ENC enables continuous updates using the latest available satellite imagery. Visual inspection further corroborates these statistical findings, illustrating the effective suppression of noise in complex agricultural landscapes (Fig. 3).

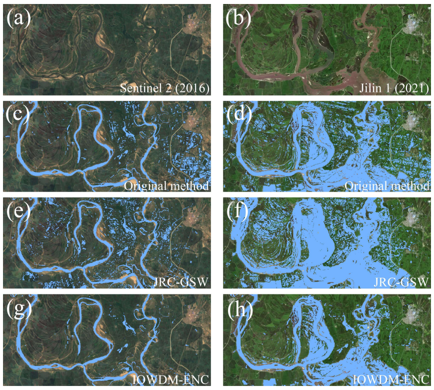

**Figure 3. Visual comparison of surface water extraction. (a) Sentinel-2 images in 2016; (b) Jilin-1 images in 2021; (c-d) Original method in 2016 and 2021; (e-f) JRC-GSW data in 2016 and 2021; (g-h) IOWDM-ENC method in 2016 and 2021.**

### 3.2 Interannual variability and divergent spatial trends

The SHRZ experienced a marked hydrological transition around the 2012 breakpoint. Before this shift, the total surface water (TSW) area showed a persistent decline (-75.21 km²/a), which reversed to a rapid expansion phase (447.87 km²/a) thereafter (Fig. 4a). This reversal coincided with a structural change in water persistence: the proportion of permanent surface water (PSW) rose from 51.92% to 69.49%, moving from an insignificant decline (-18.43 km²/a) prior to 2012 to a significant expansion (289.89 km²/a). In contrast, seasonal surface water (SSW) shifted from a significant decline (-65.97 km²/a) to a volatile but insignificant expansion (87.17 km²/a), tracking interannual precipitation variability rather than exhibiting sustained recovery (Fig. 4b, Fig. S3).

Surface water dynamics revealed distinct heterogeneity dictated by frozen ground regions. The permafrost region exhibited a " restricted recovery": while PSW rebounded significantly from a decline observed before 2012 (-21.48 km²/a) to a significant increase (63.49 km²/a), the SSW area consistently insignificant decreased (Fig. 4c). In direct contrast, the seasonal frozen ground region displayed a "concerted expansion": both PSW (208.80 km²/a) and SSW (79.14 km²/a) exhibited rapid and simultaneous growth after 2012 (Fig. 4d).

Quantitative analysis of WF reveals a total dynamic area of 5965.85 km² in the SHRZ. The portion exhibiting statistically significant changes covers 4436.87 km², representing 33.13% of the multi-year mean surface water area. Within these significant variations, expansion proved to be the dominant trend, constituting 61.09% of the altered area compared to only 13.28% for shrinkage (Table S5). A significant contrast emerges between the two frozen ground regions, the magnitude of WF increase in the seasonal frozen ground region (24.77%) exceeded that of the permafrost region (9.38%) by a factor of nearly 2.5, reflecting the divergence in spatial evolution (Table S6).

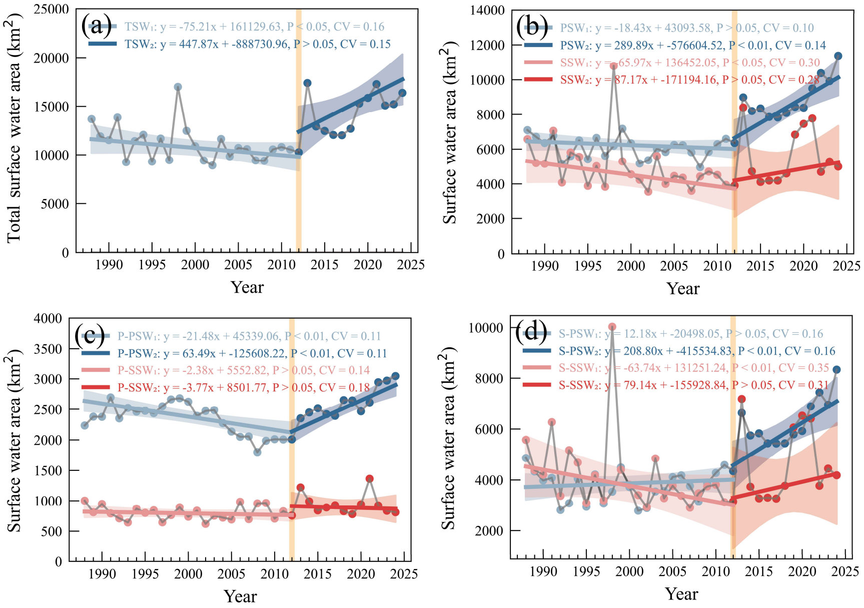

**Figure 4. Temporal dynamics of surface water area from 1988 to 2024. (a) Total surface water area in the SHRZ; (b) PSW and SSW area in the SHRZ; (c) Permafrost region; (d) seasonal frozen ground region. CV indicates the degree of data fluctuation, the shaded areas indicates the 95% confidence interval; 'P-' presents the permafrost region, 'S-' presents the seasonal frozen ground region.**

https://doi.org/10.5194/egusphere-2026-1772
Preprint. Discussion started: 29 April 2026

### 3.3 Variations in terrestrial hydrological components and surface-groundwater interactions

Interpreting surface water dynamics requires determining the state of the broader hydrological cycle. Therefore, this study
230 analyzed the evolution of three key water budget components.

Atmospheric water supply exhibited spatial heterogeneity. In the permafrost region, SWA maintained a relatively stable upward trend. The seasonal frozen ground region, by contrast, underwent a regime shift, transitioning from drying to wetting trends around 2009 (Fig. 5a); this shift provided the antecedent moisture conditions for subsequent surface water expansion.

Water storage dynamics also showed divergence after the 2012 breakpoint. While the terrestrial water storage anomaly
235 (TWSA) generally rebounded from depletion to accretion across the entire zone (Fig. 5b), GWSA entered a phase of accelerated decline. This groundwater depletion was substantially more acute in the seasonal frozen ground region than in the permafrost region (Fig. 5c), implying a disconnection between surface accumulation and aquifer recharge.

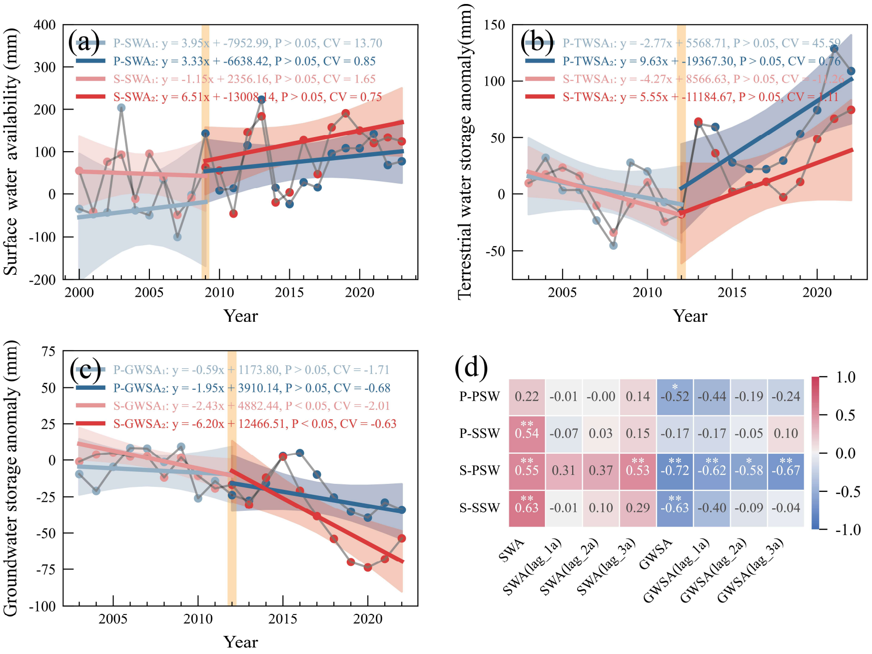

| | SWA | SWA(lag_1a) | SWA(lag_2a) | SWA(lag_3a) | GWSA | GWSA(lag_1a) | GWSA(lag_2a) | GWSA(lag_3a) |
|---|---|---|---|---|---|---|---|---|
| P-PSW | 0.22 | -0.01 | -0.00 | 0.14 | * -0.52 | -0.44 | -0.19 | -0.24 |
| P-SSW | ** 0.54 | -0.07 | 0.03 | 0.15 | -0.17 | -0.17 | -0.05 | 0.10 |
| S-PSW | ** 0.55 | 0.31 | 0.37 | ** 0.53 | ** -0.72 | ** -0.62 | * -0.58 | ** -0.67 |
| S-SSW | ** 0.63 | -0.01 | 0.10 | 0.29 | ** -0.63 | -0.40 | -0.09 | -0.04 |

**Figure 5. Interannual variability and cross-correlations of hydrological factors. (a) SWA; (b) TWSA; (c) GWSA; (d) time lagged**
240 **cross correlations, lag_1a: 1 year lag. ‘P-’ presents the permafrost region; ‘S-’ presents the seasonal frozen ground region.**

Cross-correlation analysis (Fig. 5d) clarifies the temporal coupling between these components. SSW dynamics in both regions appear largely driven by current-year SWA, with no significant lagged effects. In contrast, PSW exhibits divergent responses: it correlates strongly with current year SWA in the seasonal frozen ground region (r = 0.55) but shows a weak

https://doi.org/10.5194/egusphere-2026-1772
Preprint. Discussion started: 29 April 2026

correlation in the permafrost region (r = 0.22). Of particular importance is the significant negative correlation between PSW and concurrent GWSA across both regions. This synchronous inverse relationship provides compelling evidence of a hydrological trade-off, indicating that surface water expansion proceeds at the potential expense of groundwater storage.

### 3.4 Multi-scale attribution of PSW dynamics: From global dominance to local heterogeneity

The significant trend slopes of surface water and its driving factors (2000–2020) exhibit spatially heterogeneity (Fig. 6-7). To ensure model robustness, variables with high multicollinearity were excluded prior to analysis (Fig. 8). The framework demonstrated superior explanatory power for PSW relative to SSW (Fig. S4). This disparity is attributed to the stable nature of permanent water dynamics compared to the stochastic variability of seasonal water. Consequently, this study primarily focuses on the more deterministic PSW dynamics.

Global XGBoost SHAP analysis established a baseline ranking of driver importance (Fig. S5a–b). By calculating mean absolute SHAP values, this approach quantified the overall magnitude of influence, identifying topography and human activities as dominant contributors in the permafrost region. However, such global aggregation obscures the spatial directionality of these effects. Some drivers may act as promoting agents in some contexts and constraining agents in others (Fig. S5c–d), meaning global averaging inherently masks these opposing local mechanisms. To address this non-stationarity, this study used the spatially explicit SHAP values generated by the Geographical-XGBoost model for local attribution.

Aggregating these local effects revealed a spatial heterogeneity in regulation mechanisms across different frozen ground regions. PSW dynamics in the permafrost region were dominated by HAF, which accounted for 76.4% (Fig. 9a). By contrast, the seasonal frozen ground region was governed by a synergy of natural factors, with CEF and TSF jointly accounting for 72.4% of the dynamics (Fig. 9b). The visualization of dominant factors further confirms this spatial heterogeneity at the local scale (Fig. 10a); while TSF controlled the Heilongjiang River mainstream; the Dadingzishan and Hadashan Reservoir were jointly controlled by HAF and CEF; the lake clusters in the Songnen Plain were driven by HAF, CEF and TSF.

This heterogeneity is further substantiated by the distinct driver composition across specific water types (Fig. 9c-e). RCF exhibited the strongest anthropogenic footprint, with HAF contributing 71.0% to the total influence (Fig. 9c). Despite this overall dominance, specific drivers diverged sharply by region (Fig. 11a-b). In the permafrost region, STT had a negative influence due to the high permeability of sandy loam (Fig. 11c), which facilitates surface water infiltration (Fig. 6l). In contrast, RCF dynamics in the seasonal frozen ground region were governed by a trade-off between enhanced surface runoff facilitated by reduced vegetation cover (Fig. 6d) and the interception effects of upstream NR (Fig. 7b).

Regarding RP, while HAF (56.0%) remained the dominant driver, TSF (22.6%) and CEF (21.4%) played substantial secondary roles (Fig. 9d). This indicates that even artificial water bodies are subject to environmental constraints in the SHRZ (Fig. 11a-b). In the permafrost region, the positive influence of NR was reinforced by favorable STT (Fig. 10b), exemplified by the Nierji reservoir where low-permeability silty clay loam aids water retention (Fig. 11d). Similarly, NR played the primary role in sustaining PSW frequency within the seasonal frozen ground region.

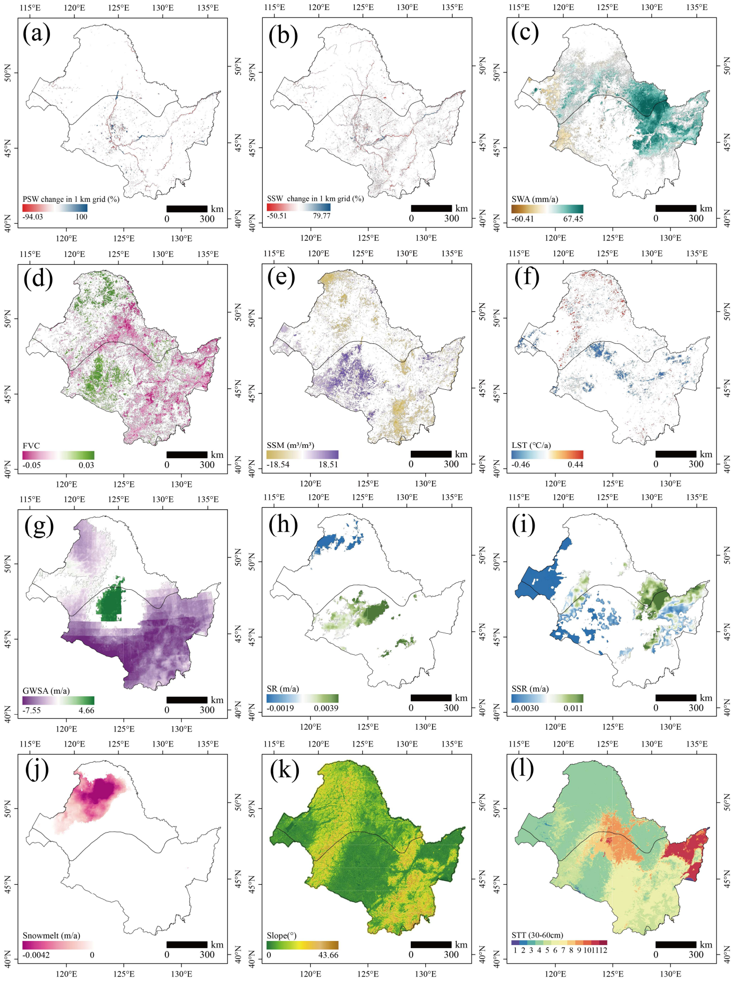

**Figure 6. The significant trend slopes for surface water and natural environmental factors in the SHRZ from 2000 to 2020. (a) PSW; (b) SSW; (c) SWA; (d) FVC; (e) SSM; (f) LST; (g) GWSA; (h) SR; (i) SSR; (j) Snowmelt; (k) Slope; (l) STT30-60cm, STT distribution: 1 = sand, 2 = loamy sand, 3 = silt, 4 = sandy loam, 5 = loam, 6 = silt loam, 7 = sandy clay loam, 8 = clay loam, 9 = silty clay loam, 10 = sandy clay, 11 = silty clay, 12 = clay.**

Finally, lake dynamics were overwhelmingly governed by natural forces, with CEF (55.7%) and TSF (37.9%) together accounting for 93.6% of the influence (Fig. 9e). This confirms that lakes serve as sensitive indicators of climate and terrain conditions rather than direct human intervention (Fig. 11a-b). Permafrost lakes primarily sustained by GWSA and SSR, indicating a dependence on groundwater recharge, while topographic barriers and HF acted as constraints (Fig. 11e). In contrast, lakes in the seasonal frozen ground region expanded through a synergistic combination of high precipitation (Fig. 5a, Fig. 6c), flat terrain (Fig. 1), and significant groundwater recovery in the Songnen Plain (Fig. 11e, Fig. 6g).

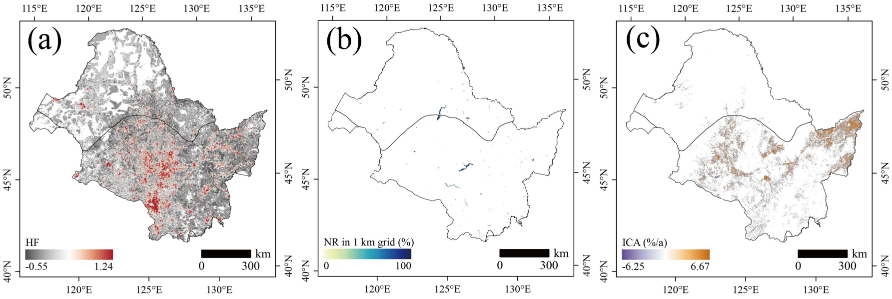

**Figure 7. The significant trend slopes for human activity factors in the SHRZ from 2000 to 2020. (a) HF; (b) NR; (c) ICA.**

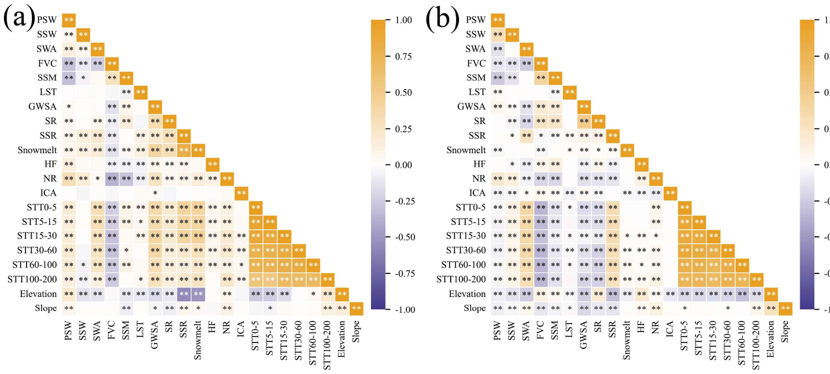

**Figure 8. Correlation analysis of the significant trend slopes of various variables in the SHRZ from 2000 to 2020. (a) Correlation analysis in the permafrost region; (b) Correlation analysis in the seasonal frozen ground region.**

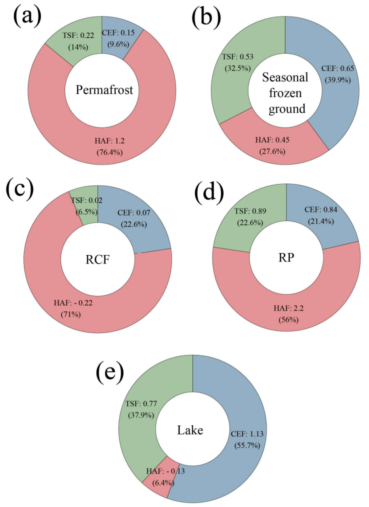

295 **Figure 9. Relative contributions of factor categories to PSW dynamics. (a–b) Permafrost and seasonal frozen ground regions; (c–e) Specific water types: RCF, RP, and Lake.**

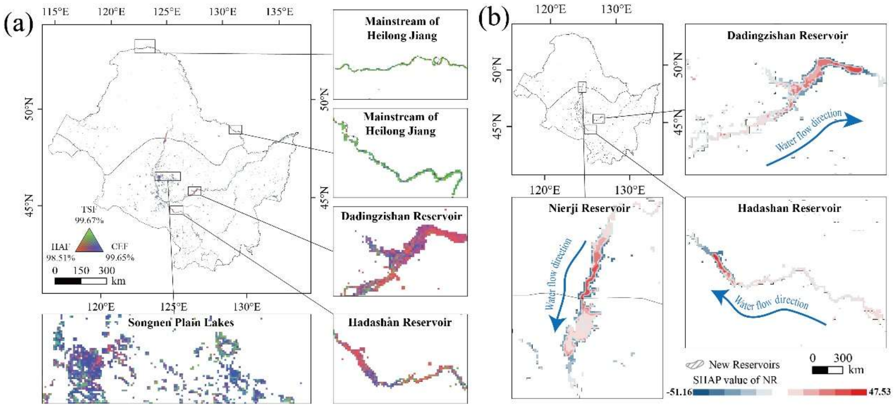

**Figure 10. Spatially explicit attribution of PSW dynamics. (a) Spatial distribution of dominant factor categories across the SHRZ; (b) Spatial heterogeneity of the NR impact on local surface water dynamics.**

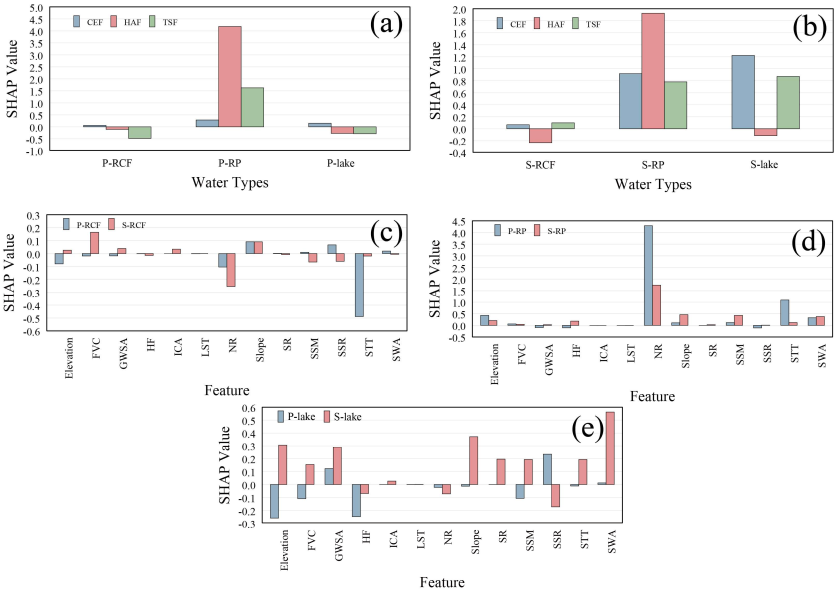

**Figure 11. Quantitative assessment of local driving mechanisms. (a–b) Aggregated impacts of factor categories for different water types in the permafrost and seasonal frozen ground regions; (c–e) Detailed local driver contributions for RCF, RP, and Lake.**

## 4 Discussion

### 4.1 Mechanistic driving surface water dynamics

The surface water dynamics in the SHRZ appears to be fundamentally governed by a mechanistic shift in SWA. The transition of SWA around 2009 from a drying to a wetting trend around 2009 (Fig. 5a) created the precondition for water expansion after 2012. This shift may be attributed to an accelerated hydrological cycle driven by climate change, which increased the SWA on average (Konapala et al., 2020). However, while increased SWA provided the necessary water surplus, the redistribution of this surplus water was critically influenced by other factors including human activities (Vörösmarty et al., 2010), topography (Song et al., 2025), soil properties (Evaristo et al., 2015), and groundwater interactions (Taylor et al., 2013) (Fig. 12a).

The ecosystem's response to extreme events reveals a structural change in water storage capacity. The 1998 flood primarily caused a rapid increase in SSW, with little impact on PSW (Fig. 4b). This phenomenon may be due to long-term cumulative flood effects (Konapala et al., 2020), for example the extensive soil saturation from frequent flood between 1980 and 2000

(Nie et al., 2012). Coupled with the inherently low hydraulic conductivity of permafrost (Walvoord and Kurylyk, 2016) and inadequate hydraulic infrastructure. This condition caused floodwater to dissipate rapidly as SSW through runoff or evapotranspiration, rather than being converted into permanent storage (Fig. 4b).

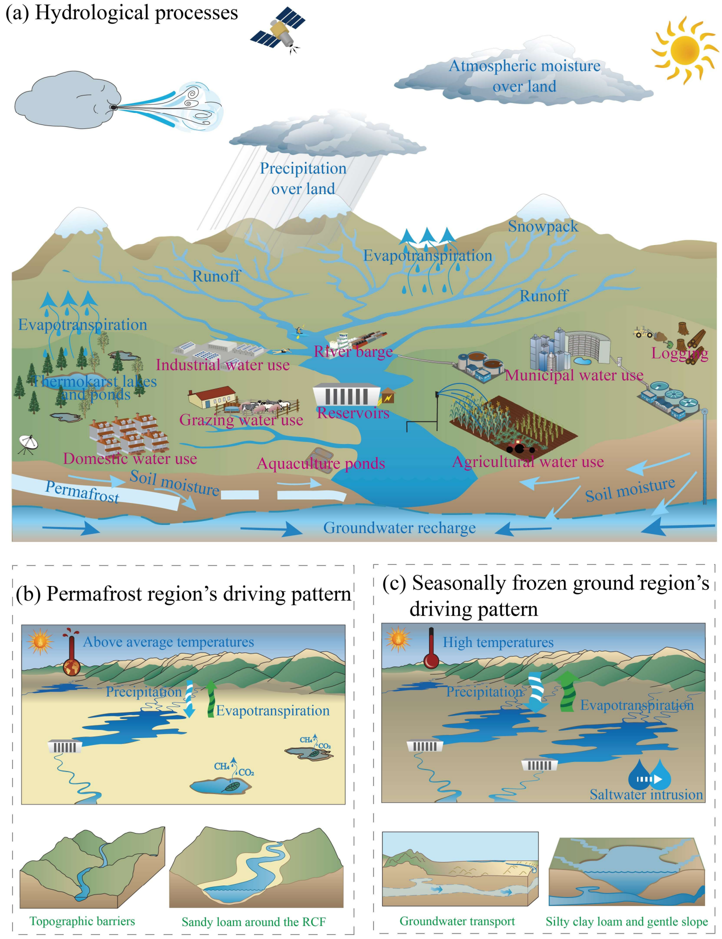

**Figure 12. Conceptual framework of hydrological mechanisms in the SHRZ. (a) Schematic of general hydrological cycle processes; (b) The "antagonistic" driving pattern in the permafrost region; (c) The "synergistic" driving pattern in the seasonal frozen ground region.**

In contrast, the 2013 flood marked an important change in water storage capacity. A rapid increase in PSW area (Fig. 4b), TWSA (Fig. 5b), and GWSA (Fig. 5c) were observed. Although the PSW area in the seasonal frozen ground region decreased slightly, it largely remained at a high level. This reflects the regulatory effect of newly constructed reservoirs and the good soil hydraulic conductivity during this period, which allowed precipitation to infiltrate rapidly into the subsurface and provide sustained recharge to PSW (Winter et al., 1998). In comparison, the increasing trend of PSW area in the permafrost region was more stable. This stability may be attributed to the accelerated thawing of the permafrost layer since 2000 (Jin et al., 2007), which enhanced the soil's water storage capacity and hydraulic conductivity (Hiyama et al., 2023). Infiltrating water flows laterally along the permafrost table, migrating into taliks and recharging groundwater (Woo and Winter, 1993). The significant increase observed in SSR in parts of the permafrost region further confirms this hydrological process (Fig. 6i, Fig. 11e).

The post-2013 period revealed a critical hydrological divergence. While PSW area and TWSA remained high, GWSA entered a phase of accelerated depletion, particularly in seasonal frozen ground regions (Fig. 5c). This decoupling suggests that while reservoir interception and soil saturation retained precipitation at the surface, intensified human water consumption led to a rapid decline in GWSA during the same period (Shang et al., 2025). This depletion was slower in the permafrost region, possibly attributable to the buffering effect of the deepening active layer, which alters groundwater flow paths and lengthens water residence times (Frampton and Destouni, 2015).

### 4.2 Divergent driving patterns of frozen ground regions

The surface water dynamics in the SHRZ exhibit two divergent patterns, driven by the intensifying influences of climate change and human activities. The permafrost region is characterized by an antagonistic pattern (Fig. 12b). The expansion of PSW is driven primarily by anthropogenic factors, particularly the construction of NR (Fig. 11a). However, this expansion faces significant environmental constraints, including limited increases in SWA (Fig. 5a), highly permeable STT (Fig. 6l), and topographic barriers (Fig. 1). Despite these constraints, the region is undergoing substantial changes due to the high sensitivity of its permafrost to warming (Chang et al., 2025). Accelerated thawing of the permafrost layer enhances the connectivity between surface and groundwater and increases subsurface storage capacity (Lamontagne-Hallé et al., 2018), which promoting surface water expansion, especially PSW. Furthermore, thaw-induced local surface subsidence promotes the formation of thermokarst lakes and ponds (Yang et al., 2016). These surface water will become increasingly important in the future hydrological dynamics of permafrost regions.

In contrast, the seasonal frozen ground region is characterized by a synergistic pattern (Fig. 12c). The increases in both SWA and NR are prerequisites for the robust expansion of PSW in this region (Fig. 11d, 11e). The synergistic effects among multiple factors of the underlying surface amplified PSW expansion and its spatial heterogeneity (Lu et al., 2023; Yin et al., 2025), which is particularly evident in the Songnen Plain lake clusters.

This synergy operates through two main pathways. First, the region's gentle slopes (Fig. 6k), low permeable STT (Fig. 6l), and high soil moisture (Fig. 6e) promote the conversion of precipitation into surface runoff (Fig. 6h). Second, the low elevation and high surface-groundwater connectivity (Fig. 1) make the Songnen Plain become the only region with a significant increase in GWSA (2000–2020), which further sustains PSW expansion (Winter et al., 1998; Kløve et al., 2011). Stable isotope studies support this mechanism, confirming that the plain's surface water is replenished by both precipitation and groundwater inflow from mountainous areas (Zhang et al., 2015) , and that lakes heavily depend on groundwater recharge during dry seasons (Liu et al., 2025). Overall, the rapid expansion of PSW in the seasonal frozen ground region results from a favorable combination of multiple driving factors. But this synergy is associated with a high ecological cost: groundwater resources become more difficult to replenish under increasing human consumption.

From a broader perspective, the contrasting "antagonistic" and "synergistic" patterns identified in this study are not merely local phenomena. As permafrost degradation accelerates across the Northern Hemisphere (Chadburn et al., 2017), the hydrological consequences are highly divergent due to the local hydrological controls (Walvoord and Kurylyk, 2016). This divergence presents challenge for future water security, as thawing ground can influence water quality, ecosystems and infrastructure (Colombo et al., 2018). This study demonstrates the urgent need for spatially explicit models to manage the future of earth's water resources in a rapidly thawing world.

### 4.3 Limitations and perspectives

This study has several limitations concerning data constraints and scale effects. First, while the IOWDM-ENC is accurate, optical remote sensing is inherently affected by uncertainties from mixed pixels and cloud cover (Wang et al., 2025). Second, the necessary step of resampling multiple driver datasets to a uniform 1 km grid inevitably smoothed fine-scale process variations (Gotway and Young, 2002). Due to data availability constraints, this study relied on static permafrost maps rather than dynamic variables like active layer thickness (Walvoord and Kurylyk, 2016). This limits the real-time quantification of cryospheric feedbacks. Future research that integrates process-based permafrost models with high-resolution remote sensing data could address these mechanistic gaps.

Despite these are some limitations, this study demonstrates the value of explainable GeoAI in dissecting complex environmental mechanisms. Unlike conventional "black-box" models that output only global importance rankings, the Geographical-XGBoost-SHAP framework resolves spatially heterogeneous effects. The impact of reservoir regulation provides a clear example: the model identified that NR generally promoted PSW expansion in the SHRZ, they also exerted a significant negative impact on downstream water stability (Fig. 10b). This finding aligns with recent research on the hydrological fragmentation caused by dam construction (Fan et al., 2025).

These findings bear direct implications for the realm of sustainable water management. In seasonal frozen ground regions, such as the Songnen Plain, the contrast between "synergistic" surface water expansion and accelerated groundwater depletion indicates the necessity for conjunctive water use strategies. Such strategies should entail the utilization of the expanded surface water from reservoirs and lakes to substitute for deep groundwater in irrigation, while concurrently investigating ecological replenishment for rivers and lakes and managed aquifer recharge. Conversely, in permafrost regions where the "antagonistic" pattern structurally limits water body expansion, management should focus on mitigating the downstream hydrological disturbances of engineering projects. The implementation of ecologically informed reservoir scheduling is imperative for the preservation of ecosystem resilience along this climate-sensitive permafrost margin.

## 5 Conclusion

This study advances the understanding of ecohydrological dynamics and provides a spatially explicit attribution of the divergent hydrological responses at the southern permafrost margin by integrating a high-precision monitoring dataset with an interpretable GeoAI framework. The main conclusions are summarized as follows:

(1) The IOWDM-ENC demonstrated more superior applicability than existing methods in the SHRZ, achieving an overall accuracy of 99.03%. From 1988 to 2024, the SHRZ experienced a marked hydrological reversal from shrinkage to expansion. Using 1988 as the baseline year, surface water increased by 9.38% in the permafrost region and by 24.77% in the seasonal frozen ground region.

(2) The Geographical-XGBoost-SHAP framework effectively resolved the stationarity limitations of global-scale models. Rather than assuming a uniform influence, this spatially explicit GeoAI framework quantitatively identifying specific locations where factors function as promoters or inhibitors. This capability provides a reliable technical basis for revealing localized hydrological controls that vary significantly across this complex permafrost margin.

(3) Surface water dynamics are governed by distinct regulation mechanisms. At the regional scale, a divergence exists between the antagonistic pattern in the permafrost region (where permanent water expansion is constrained by environmental barriers) and the synergistic pattern in the seasonal frozen ground region (where climate, terrain, and human factors amplify expansion). At the typological scale, permanent lake dynamics are primarily controlled by natural factors (55.7% CEF and 37.9% TSF). In contrast, anthropogenic factors dominate both RCF (71.0%) and RP (56.0%), while exerting opposing influences by constraining RCF expansion but promoting RP

https://doi.org/10.5194/egusphere-2026-1772
Preprint. Discussion started: 29 April 2026

expansion.

(4) The hydrological trade-off emerged between surface water expansion and groundwater storage depletion. The observed increase in surface water area coincides with a decline in GWSA, suggesting that surface water expansion has occurred at the potential expense of subsurface storage. This trade-off is particularly significant in the seasonal frozen ground region, highlighting the urgent need for surface-groundwater management strategies tailored to the distinct regulation mechanisms identified in this study.

## Data availability

The China Water Resources Bulletin of 2024 is available at Ministry of Water Resources of the People's Republic of China (http://www.mwr.gov.cn/sj/tjgb/szygb/202506/t20250610_1732735.html). National Water Resources Zones classification is available at National Earth System Science Data Center (https://www.geodata.cn/data/datadetails.html?dataguid=243293730193084&docid=1831). The distribution map of frozen ground in China based on the map of snow, ice and frozen ground in China is available at National Cryosphere Desert Data Center (https://www.ncdc.ac.cn/portal/metadata/69078ce0-4d34-40fd-8d74-176e96fd902d). GWSA and TWSA dataset are available at National Tibetan Plateau Data Center (https://doi.org/10.11888/Terre.tpdc.300962.). SWA dataset is available at National Tibetan Plateau Data Center (https://doi.org/10.5281/zenodo.3114194., https://doi.org/10.11888/Terre.tpdc.272389). FVC dataset is available at Earthdata (https://doi.org/10.5067/MODIS/MOD13A2.061). LST dataset is available at Earthdata (https://doi.org/10.5067/MODIS/MOD11A2.061). SSM dataset is available at National Tibetan Plateau Data Center (https://doi.org/10.11888/RemoteSen.tpdc.272760.). SR and SSR dataset are available at Copernicus Climate Data Store (https://doi.org/10.24381/cds.e9c9c792). STT dataset is available at National Earth System Science Data Center (https://doi.org/10.11666/00073.ver1.db). The elevation and slope data are available at Earthdata (https://doi.org/10.5067/MEaSUREs/SRTM/SRTMGL1.003). NR dataset is available at National Earth System Science Data Center (https://doi.org/10.57760/sciencedb.15520). HF dataset is available at the College of Land Science and Technology, China Agricultural University (https://www.x-mol.com/groups/li_xuecao/news/48145). ICA dataset is available at National Cryosphere Desert Data Center (https://doi.org/10.6084/m9.figshare.24814293.v2). CNLUCC dataset is available at Resource and Environmental Science Data Platform (https://doi.org/10.12078/2018070201). GMTED2010 dateset is available at United States Geological Survey (https://www.usgs.gov/coastal-changes-and-impacts/gmted2010). GAIA dateset is available at iEarth DataHub of Peng Cheng Laboratory (https://data-starcloud.pcl.ac.cn/iearthdata/13).

## Author contributions

**Bo Zhang**: Conceptualization, Data curation, Formal analysis, Investigation, Methodology, Software, Validation, Visualization, Writing – original draft. **Tiantian Liao**: Conceptualization, Validation, Writing – original draft. **Haitian Lu**:

Methodology, Formal analysis. **Jianuo Li**: Methodology, Software. **Ziyan Huang**: Formal analysis, Writing – review & editing. **Jiuhui Li**: Funding acquisition, Methodology, Supervision, Writing review & editing. **Meng Guo**: Conceptualization, Funding acquisition, Project administration, Resources, Supervision, Writing review & editing. All authors reviewed, edited and approved the final version of the manuscript.

## Competing interests

The authors declare that they have no conflict of interest.

## Acknowledgements

We are grateful to the National Natural Science Foundation of China.

## Financial support

This work was supported by the National Natural Science Foundation of China (42371098, 4220020142).

## References

Box, G. E. P., Jenkins, G. M., Reinsel, G. C., and Ljung, G. M.: Time Series Analysis: Forecasting and Control, Wiley, Hoboken, New Jersey, 720 pp., 2016.

Brunsdon, C., Fotheringham, A. S., and Charlton, M. E.: Geographically Weighted Regression: A Method for Exploring Spatial Nonstationarity, Geogr. Anal., 28, 281–298, https://doi.org/10.1111/j.1538-4632.1996.tb00936.x, 1996.

Chadburn, S. E., Burke, E. J., Cox, P. M., Friedlingstein, P., Hugelius, G., and Westermann, S.: An observation-based constraint on permafrost loss as a function of global warming, Nat. Clim. Chang., 7, 340–344, https://doi.org/10.1038/nclimate3262, 2017.

Chang, Q., Zwieback, S., and Berg, A.: Trends and drivers of Arctic lake color change from Landsat time series, Int. J. Appl. Earth Obs. Geoinf., 145, 104952, https://doi.org/10.1016/j.jag.2025.104952, 2025.

Colombo, N., Salerno, F., Gruber, S., Freppaz, M., Williams, M., Fratianni, S., and Giardino, M.: Review: Impacts of permafrost degradation on inorganic chemistry of surface fresh water, Glob. Planet. Change, 162, 69–83, https://doi.org/10.1016/j.gloplacha.2017.11.017, 2018.

Copernicus Climate Change Service: ERA5-Land monthly averaged data from 1950 to present, https://doi.org/10.24381/CDS.68D2BB30, 2019.

Cui, J., Lian, X., Huntingford, C., Gimeno, L., Wang, T., Ding, J., He, M., Xu, H., Chen, A., Gentine, P., and Piao, S.: Global water availability boosted by vegetation-driven changes in atmospheric moisture transport, Nat. Geosci., 15, 982–988, https://doi.org/10.1038/s41561-022-01061-7, 2022.

Danielson, J. J. and Gesch, D. B.: Global multi-resolution terrain elevation data 2010 (GMTED2010), Open-File Report, U.S. Geological Survey, https://doi.org/10.3133/ofr20111073, 2011.

Didan, K.: MODIS/Terra Vegetation Indices 16-Day L3 Global 1km SIN Grid V061, https://doi.org/10.5067/MODIS/MOD13A2.061, 2021.

Dormann, C. F., Elith, J., Bacher, S., Buchmann, C., Carl, G., Carré, G., Marquéz, J. R. G., Gruber, B., Lafourcade, B., Leitão, P. J., Münkemüller, T., McClean, C., Osborne, P. E., Reineking, B., Schröder, B., Skidmore, A. K., Zurell, D., and Lautenbach, S.: Collinearity: a review of methods to deal with it and a simulation study evaluating their performance, Ecography, 36, 27–46, https://doi.org/10.1111/j.1600-0587.2012.07348.x, 2013.

Evaristo, J., Jasechko, S., and McDonnell, J. J.: Global separation of plant transpiration from groundwater and streamflow, Nature, 525, 91–94, https://doi.org/10.1038/nature14983, 2015.

Fan, C., Song, C., Wang, J., Sheng, Y., Lin, Y., Yuan, C., Sikder, S., Crétaux, J.-F., Liu, K., Chen, T., Zeng, F., and Ke, L.: Emerging global reservoirs in the new millennium: Abundance, hotspots, and total water storage, Sci. Bull., 69, 2179–2182, https://doi.org/10.1016/j.scib.2024.04.043, 2024.

Fan, C., Ke, L., Wang, J., Best, J., Zhang, Y., Sheng, Y., Liu, K., Chen, T., Zeng, F., Zhan, P., Zhu, J., Cheng, J., and Song, C.: Exacerbating dam-induced fragmentation in China's river systems, Commun. Earth Environ., 6, 428, https://doi.org/10.1038/s43247-025-02416-9, 2025.

Farr, T. G., Rosen, P. A., Caro, E., Crippen, R., Duren, R., Hensley, S., Kobrick, M., Paller, M., Rodriguez, E., Roth, L., Seal, D., Shaffer, S., Shimada, J., Umland, J., Werner, M., Oskin, M., Burbank, D., and Alsdorf, D.: The Shuttle Radar Topography Mission, Rev. Geophys., 45, https://doi.org/10.1029/2005RG000183, 2007.

Foga, S., Scaramuzza, P. L., Guo, S., Zhu, Z., Dilley, R. D., Beckmann, T., Schmidt, G. L., Dwyer, J. L., Joseph Hughes, M., and Laue, B.: Cloud detection algorithm comparison and validation for operational Landsat data products, Remote Sens. Environ., 194, 379–390, https://doi.org/10.1016/j.rse.2017.03.026, 2017.

Frampton, A. and Destouni, G.: Impact of degrading permafrost on subsurface solute transport pathways and travel times, Water Resour. Res., 51, 7680–7701, https://doi.org/10.1002/2014WR016689, 2015.

Frampton, A., Painter, S. L., and Destouni, G.: Permafrost degradation and subsurface-flow changes caused by surface warming trends, Hydrogeol. J., 21, 271–280, https://doi.org/10.1007/s10040-012-0938-z, 2013.

Gardner, R. C., Barchiesi, S., Beltrame, C., Finlayson, C. M., Galewski, T., Harrison, I., Paganini, M., Perennou, C., Pritchard, D., Rosenqvist, A., and Walpole, M.: State of the World's Wetlands and Their Services to People: A Compilation of Recent Analyses, SSRN Journal, https://doi.org/10.2139/ssrn.2589447, 2015.

Gong, P., Li, X., Wang, J., Bai, Y., Chen, B., Hu, T., Liu, X., Xu, B., Yang, J., Zhang, W., and Zhou, Y.: Annual maps of global artificial impervious area (GAIA) between 1985 and 2018, Remote Sens. Environ., 236, 111510, https://doi.org/10.1016/j.rse.2019.111510, 2020.

Gotway, C. A. and Young, L. J.: Combining Incompatible Spatial Data, J. Am. Stat. Assoc., 97, 632–648, https://doi.org/10.1198/016214502760047140, 2002.

Grekousis, G.: Geographical-XGBoost: a new ensemble model for spatially local regression based on gradient-boosted trees, J. Geogr. Syst., 27, 169–195, https://doi.org/10.1007/s10109-025-00465-4, 2025.

Hawkins, D. M. and Olwell, D. H.: Cumulative Sum Charts and Charting for Quality Improvement, Springer, New York, NY, 263 pp., 1998.

He, S., Zhang, Y., Ma, N., Tian, J., Kong, D., and Liu, C.: A daily and 500m coupled evapotranspiration and gross primary production product across China during 2000–2020, Earth Syst. Sci. Data, 14, 5463–5488, https://doi.org/10.5194/essd-14-5463-2022, 2022.

Heginbottom, J., Brown, J., Ferrians, O., and Melnikov, E. S.: Circum-Arctic Map of Permafrost and Ground-Ice Conditions, Version 2, https://doi.org/10.7265/SKBG-KF16, 2002.

Hiyama, T., Park, H., Kobayashi, K., Lebedeva, L., and Gustafsson, D.: Contribution of summer net precipitation to winter river discharge in permafrost zone of the Lena River basin, J. Hydrol., 616, 128797, https://doi.org/10.1016/j.jhydrol.2022.128797, 2023.

Huete, A. R., Liu, H. Q., Batchily, K., and van Leeuwen, W.: A comparison of vegetation indices over a global set of TM images for EOS-MODIS, Remote Sens. Environ., 59, 440–451, https://doi.org/10.1016/S0034-4257(96)00112-5, 1997.

Jin, H., Yu, Q., Lü, L., Guo, D., He, R., Yu, S., Sun, G., and Li, Y.: Degradation of permafrost in the Xing'anling Mountains, northeastern China, Permafrost Periglacial Process., 18, 245–258, https://doi.org/10.1002/ppp.589, 2007.

Kløve, B., Ala-aho, P., Bertrand, G., Boukalova, Z., Ertürk, A., Goldscheider, N., Ilmonen, J., Karakaya, N., Kupfersberger, H., Kvœrner, J., Lundberg, A., Mileusnić, M., Moszczynska, A., Muotka, T., Preda, E., Rossi, P., Siergieiev, D., Šimek, J., Wachniew, P., Angheluta, V., and Widerlund, A.: Groundwater dependent ecosystems. Part I: Hydroecological status and trends, Environ. Sci. Policy, 14, 770–781, https://doi.org/10.1016/j.envsci.2011.04.002, 2011.

Konapala, G., Mishra, A. K., Wada, Y., and Mann, M. E.: Climate change will affect global water availability through compounding changes in seasonal precipitation and evaporation, Nat. Commun., 11, 3044, https://doi.org/10.1038/s41467-020-16757-w, 2020.

Lamontagne-Hallé, P., McKenzie, J. M., Kurylyk, B. L., and Zipper, S. C.: Changing groundwater discharge dynamics in permafrost regions, Environ. Res. Lett., 13, 084017, https://doi.org/10.1088/1748-9326/aad404, 2018.

Li, F., Zhang, G., and Xu, Y. J.: Spatiotemporal variability of climate and streamflow in the Songhua River Basin, northeast China, J. Hydrol., 514, 53–64, https://doi.org/10.1016/j.jhydrol.2014.04.010, 2014.

Li, J.Y., Liu, J.F., Qu, J.F., Zheng, R.G., Zhao, S., Zhang, J., Sun, L.X., Li, Y.F., Yang, X.P., Wang, L.J., and Zhang, X.W.: Major geological features and crustal tectonic framework of Northeast China, Acta Petrol. Sin., 35, 2989-3016, doi:10.18654/1000-0569/2019. 10.04, 2019.

Liang, H., Zhou, Y., Cui, Y., Dong, J., Gao, Z., Liu, B., and Xiao, X.: Is satellite-observed surface water expansion a good signal to China’s largest granary?, Agric. Water Manage., 303, 109039, https://doi.org/10.1016/j.agwat.2024.109039, 2024.

Liu, F., Wu, H., Zhao, Y., Li, D., Yang, J.-L., Song, X., Shi, Z., Zhu, A.-X., and Zhang, G.-L.: Mapping high resolution National Soil Information Grids of China, Sci. Bull., 67, 328–340, https://doi.org/10.1016/j.scib.2021.10.013, 2022.

Liu, K., Zhang, D., Chen, T., Cui, P., Fan, C., and Song, C.: Monitoring Surface Water Change in Northeast China in 1999–2020: Evidence from Satellite Observation and Refined Classification, Chin. Geogr. Sci., 34, 106–117, https://doi.org/10.1007/s11769-024-1411-3, 2024.

Liu, Z., Wang, X., Jun Xu, Y., Mao, B., Jia, S., Wang, C., Lv, Q., and Ji, X.: Multi-indicators to investigate the spatiotemporal effect of groundwater-lake interaction on lake development: Case study in the largest fresh water lake (Poyang Lake) of China, J. Hydrol., 650, 132557, https://doi.org/10.1016/j.jhydrol.2024.132557, 2025.

Lu, H., Zhao, R., Zhao, L., Lyu, B., Wang, J., and Zhang, L.: A contrarian growth: The spatiotemporal dynamics of open-surface water bodies on the northern slope of Kunlun Mountains, Ecol. Indic., 157, 111249, https://doi.org/10.1016/j.ecolind.2023.111249, 2023a.

Lu, H., Zhao, R., Zhao, L., Liu, J., Lyu, B., and Yang, X.: Impact of climate change and human activities on the spatiotemporal dynamics of surface water area in Gansu Province, China, J. Arid Land, 16, 798–815, https://doi.org/10.1007/s40333-024-0078-z, 2024.

Lu, S., Bai, X., Zhang, J., Li, J., Li, W., and Lin, J.: Impact of virtual water export on water resource security associated with the energy and food bases in Northeast China, Technological Forecasting and Social Change, 180, 121635, https://doi.org/10.1016/j.techfore.2022.121635, 2022.

Lu, Z., Li, K., Zhang, J., Lei, G., Yu, Z., and Li, C.: Mechanisms influencing changes in water cycle processes in the changing environment of the Songnen Plain, China, Sci. Total Environ., 905, 166916, https://doi.org/10.1016/j.scitotenv.2023.166916, 2023b.

Lundberg, S. M. and Lee, S.-I.: A Unified Approach to Interpreting Model Predictions, in: Advances in Neural Information Processing Systems, 2017.

Mu, H., Li, X., Wen, Y., Huang, J., Du, P., Su, W., Miao, S., and Geng, M.: A global record of annual terrestrial Human Footprint dataset from 2000 to 2018, Sci. Data, 9, 176, https://doi.org/10.1038/s41597-022-01284-8, 2022.

Nie, C., Li, H., Yang, L., Wu, S., Liu, Y., and Liao, Y.: Spatial and temporal changes in flooding and the affecting factors in China, Nat. Hazards, 61, 425–439, https://doi.org/10.1007/s11069-011-9926-1, 2012.

Olofsson, P., Foody, G. M., Stehman, S. V., and Woodcock, C. E.: Making better use of accuracy data in land change studies: Estimating accuracy and area and quantifying uncertainty using stratified estimation, Remote Sens. Environ., 129, 122–131, https://doi.org/10.1016/j.rse.2012.10.031, 2013.

Olofsson, P., Foody, G. M., Herold, M., Stehman, S. V., Woodcock, C. E., and Wulder, M. A.: Good practices for estimating area and assessing accuracy of land change, Remote Sens. Environ., 148, 42–57, https://doi.org/10.1016/j.rse.2014.02.015, 2014.

Pekel, J.-F., Cottam, A., Gorelick, N., and Belward, A. S.: High-resolution mapping of global surface water and its long-term changes, Nature, 540, 418–422, https://doi.org/10.1038/nature20584, 2016.

Peng, S., Ding, Y., Liu, W., and Li, Z.: 1km monthly temperature and precipitation dataset for China from 1901 to 2017, Earth Syst. Sci. Data, 11, 1931–1946, https://doi.org/10.5194/essd-11-1931-2019, 2019.

Reichstein, M., Camps-Valls, G., Stevens, B., Jung, M., Denzler, J., Carvalhais, N., and Prabhat: Deep learning and process understanding for data-driven Earth system science, Nature, 566, 195–204, https://doi.org/10.1038/s41586-019-0912-1, 2019.

Rokni, K., Ahmad, A., Solaimani, K., and Hazini, S.: A new approach for surface water change detection: Integration of pixel level image fusion and image classification techniques, Int. J. Appl. Earth Obs. Geoinf., 34, 226–234, https://doi.org/10.1016/j.jag.2014.08.014, 2015.

Samaniego, L.: Permanent shifts in the global water cycle, Science, 387, 1348–1350, https://doi.org/10.1126/science.adw5851, 2025.

Sen, P. K.: Estimates of the Regression Coefficient Based on Kendall's Tau, J. Am. Stat. Assoc., 63, 1379–1389, https://doi.org/10.1080/01621459.1968.10480934, 1968.

Shang, Y., Dong, J., Fu, P., You, N., Zhang, X., Di, Y., Zhou, Y., Chen, X., Li, Z., and Zheng, X.: Groundwater depletion in China's Granary: The unintended consequences of cropping pattern shifts, J. Hydrol., 662, 134012, https://doi.org/10.1016/j.jhydrol.2025.134012, 2025.

Song, C., He, H. S., Chang, S., and Liu, K.: Wetlands change in mid to high latitude region from the perspectives of patch and landscape scales, J. Hydrol., 661, 133777, https://doi.org/10.1016/j.jhydrol.2025.133777, 2025.

Tamiminia, H., Salehi, B., Mahdianpari, M., Quackenbush, L., Adeli, S., and Brisco, B.: Google Earth Engine for geo-big data applications: A meta-analysis and systematic review, ISPRS-J. Photogramm. Remote Sens., 164, 152–170, https://doi.org/10.1016/j.isprsjprs.2020.04.001, 2020.

Taylor, R. G., Scanlon, B., Döll, P., Rodell, M., van Beek, R., Wada, Y., Longuevergne, L., Leblanc, M., Famiglietti, J. S., Edmunds, M., Konikow, L., Green, T. R., Chen, J., Taniguchi, M., Bierkens, M. F. P., MacDonald, A., Fan, Y., Maxwell, R. M., Yechieli, Y., Gurdak, J. J., Allen, D. M., Shamsudduha, M., Hiscock, K., Yeh, P. J.-F., Holman, I., and Treidel, H.: Ground water and climate change, Nat. Clim. Chang., 3, 322–329, https://doi.org/10.1038/nclimate1744, 2013.

Vörösmarty, C. J., McIntyre, P. B., Gessner, M. O., Dudgeon, D., Prusevich, A., Green, P., Glidden, S., Bunn, S. E., Sullivan, C. A., Liermann, C. R., and Davies, P. M.: Global threats to human water security and river biodiversity, Nature, 467, 555–561, https://doi.org/10.1038/nature09440, 2010.

Walvoord, M. A. and Kurylyk, B. L.: Hydrologic Impacts of Thawing Permafrost—A Review, Vadose Zone J., 15, vzj2016.01.0010, https://doi.org/10.2136/vzj2016.01.0010, 2016.

Wan, Z., Hook, S., and Hulley, G.: MODIS/Terra Land Surface Temperature/Emissivity 8-Day L3 Global 1km SIN Grid V061, https://doi.org/10.5067/MODIS/MOD11A2.061, 2021.

Wang, Y., Xin, Z., Zhang, C., Han, P., Pi, X., and Song, C.: Revealing lake dynamics across the Amur River Basin over the past two decades using multi-source remote sensing datasets, J. Hydrol.-Reg. Stud., 55, 101928, https://doi.org/10.1016/j.ejrh.2024.101928, 2024.

Wang, Z., Huang, Y., Jia, X., Hao, Z., Li, S., Zhang, L., Du, Y., and Ling, F.: Mapping long-term surface water dynamics by integrating fine resolution binary maps and medium resolution fraction series, J. Hydrol., 661, 133555, https://doi.org/10.1016/j.jhydrol.2025.133555, 2025.

Winter, T. C., Harvey, J. W., Franke, O. L., and Alley, W. M.: Ground water and surface water: A single resource, Circular, U.S. Geological Survey, https://doi.org/10.3133/cir1139, 1998.

Woo, M.-K. and Winter, T. C.: The role of permafrost and seasonal frost in the hydrology of northern wetlands in North America, J. Hydrol., 141, 5–31, https://doi.org/10.1016/0022-1694(93)90043-9, 1993.

Wu, G. and Liu, Y.: Capturing variations in inundation with satellite remote sensing in a morphologically complex, large lake, J. Hydrol., 523, 14–23, https://doi.org/10.1016/j.jhydrol.2015.01.048, 2015.

Wu, Q., Lane, C. R., Li, X., Zhao, K., Zhou, Y., Clinton, N., DeVries, B., Golden, H. E., and Lang, M. W.: Integrating LiDAR data and multi-temporal aerial imagery to map wetland inundation dynamics using Google Earth Engine, Remote Sens. Environ., 228, 1–13, https://doi.org/10.1016/j.rse.2019.04.015, 2019.

Wu, Y., Zhang G.: Spatio-temporal Patterns of Meteorological and Hydrological Drought in the Songhua River Area from 1961 to 2010, Sci. Geogr. Sin., 38, 1731-1739. https://doi.org/10.13249/j.cnki.sgs.2018.10.018, 2018.

Xu, H.: Modification of normalised difference water index (NDWI) to enhance open water features in remotely sensed imagery, Int. J. Remote Sens., 27, 3025–3033, https://doi.org/10.1080/01431160600589179, 2006.

Yang, H., Xing, Y., Chang, X., Wang, J., Li, Y., Tang, J., and Wang, D.: Internal response of vegetation growth to degrees of permafrost degradation in Northeast China from 2001 to 2020, Geo-Spat. Inf. Sci., 28, 265–283, https://doi.org/10.1080/10095020.2024.2363618, 2025.

Yang, Y., Wu, Q., Yun, H., Jin, H., and Zhang, Z.: Evaluation of the hydrological contributions of permafrost to the thermokarst lakes on the Qinghai–Tibet Plateau using stable isotopes, Glob. Planet. Change, 140, 1–8, https://doi.org/10.1016/j.gloplacha.2016.03.006, 2016.

Yin, X., Shu, L., Wang, Z., Li, Y., Zhou, L., Lv, C., Li, S., Liu, B., and Lu, C.: Quantifying the time-varying period and time lag features of groundwater response: Dynamic impacts of precipitation-fed groundwater recharge, Ecol. Indic., 176, 113648, https://doi.org/10.1016/j.ecolind.2025.113648, 2025.

Yu, B., Cui, B., Zang, Y., Wu, C., Zhao, Z., and Wang, Y.: Long-Term Dynamics of Different Surface Water Body Types and Their Possible Driving Factors in China, Remote Sens., 13, 1154, https://doi.org/10.3390/rs13061154, 2021.

Zhang, B., Song, X., Zhang, Y., Han, D., Tang, C., Yang, L., and Wang, Z.-L.: The relationship between and evolution of surface water and groundwater in Songnen Plain, Northeast China, Environ. Earth Sci., 73, 8333–8343, https://doi.org/10.1007/s12665-014-3995-x, 2015.

Zhang, G., Xu, T., Yin, W., Bateni, S. M., Jun, C., Kim, D., Liu, S., Xu, Z., Ming, W., and Wang, J.: A machine learning downscaling framework based on a physically constrained sliding window technique for improving resolution of global water storage anomaly, Remote Sens. Environ., 313, 114359, https://doi.org/10.1016/j.rse.2024.114359, 2024a.

Zhang, L., Zhang, K., Zhu, X., Chen, H., and Wang, W.: Integrating remote sensing, irrigation suitability and statistical data for irrigated cropland mapping over mainland China, J. Hydrol., 613, 128413, https://doi.org/10.1016/j.jhydrol.2022.128413, 2022.

Zhang, L., Xie, Y., Zhu, X., Ma, Q., and Brocca, L.: CIrrMap250: annual maps of China's irrigated cropland from 2000 to 2020 developed through multisource data integration, Earth Syst. Sci. Data, 16, 5207–5226, https://doi.org/10.5194/essd-16-5207-2024, 2024b.

Zheng, A. and Casari, A.: Feature Engineering for Machine Learning: Principles and Techniques for Data Scientists, O'Reilly Media, Beijing : Boston, 215 pp., 2018.

Zheng, C., Jia, L., and Zhao, T.: A 21-year dataset (2000–2020) of gap-free global daily surface soil moisture at 1-km grid resolution, Sci. Data, 10, 139, https://doi.org/10.1038/s41597-023-01991-w, 2023.

Zhou, H., Qiu, J., Li, M., Lu, H., and Li, F.: Assessment of Large-Scale Reservoirs' Impact on the Local Precipitation, Water Resour. Res., 61, e2025WR039938, https://doi.org/10.1029/2025WR039938, 2025.

Zou, Z., Xiao, X., Dong, J., Qin, Y., Doughty, R. B., Menarguez, M. A., Zhang, G., and Wang, J.: Divergent trends of open-surface water body area in the contiguous United States from 1984 to 2016, Proc. Natl. Acad. Sci. U. S. A., 115, 3810–3815, https://doi.org/10.1073/pnas.1719275115, 2018.